Nanoscale

Accepted Manuscript

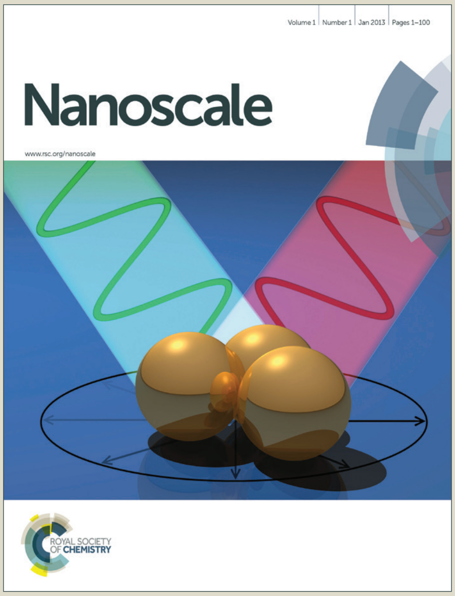

www.rsc.org/nanoscale

Cite this: DOI: 10.1039/c0xx00000x

www.rsc.org/xxxxxx

ARTICLE TYPE

Synthesis of dendritic iridium nanostructures based on the oriented attachment mechanism and their enhanced CO and ammonia catalytic activities

Chao Wang,[a] Guanjun Xiao,[a] Yongming Sui,*[a] Xinyi Yang,[a] Gang Liu,[b] Mingjun Jia,[b] Wei Han,[c] Bingbing Liu[a] and Bo Zou*[a]

Received (in XXX, XXX) Xth XXXXXXXXX 20XX, Accepted Xth XXXXXXXXX 20XX
DOI: 10.1039/b000000x

Branched Iridium nanodendrites (Ir NDs) have been synthesized by a simple method based on the oriented attachment mechanism. Transmission electron microscopy images reveal the temporal growth process from small particles to NDs. Precursor concentrations and reaction temperatures have a limited effect on the morphology of Ir NDs. Metal oxide and hydroxide-supported Ir NDs exhibit enhanced activity for the CO catalytic oxidation. Particularly, the $Fe(OH)_x$-supported Ir NDs catalyst with a 4% Ir loading show superior CO oxidation catalytic activity with a full conversion of CO at 120 °C. Furthermore, compared with Ir NPs and commercial Ir black, Ir NDs exhibit higher activity and stability for the ammonia oxidation. The specific activity and mass activity of Ir NDs for ammonia oxidation are 1.7 and 7 times higher than that of Ir NPs. The improved catalytic activities of Ir NDs are attributed not only to their large specific surface area, but also to their plentiful high index facets and rich edge and corner atoms. Hence, the obtained Ir NDs provides a promising alternative for direct ammonia fuel cells and proton-exchange membrane fuel cells.

Introduction

Metal nanostructures have attracted considerable interests owing to their preferable properties and potential applications in electronics,[1] sensing,[2, 3] medicine,[4, 5] imaging,[6, 7] especially in the field of catalysis.[8-11] In the past decades, in particular, a large amount of Pd,[12-14] Ru,[15] Rh,[16, 17] Pt,[18, 19] Au,[20] and Ru-Pt bimetallic[21] catalysts have shown superior activities in both homogeneous and heterogeneous reactions. Iridium (Ir), like other noble metals, shows a wide variety of potential applications in the field of catalysis for many chemical reactions. For example, Ir catalysts were used for asymmetric allylic substitutions,[22] enantioselective synthesis of allylic alcohols,[23] and oxidation of CO.[24, 25] B. C. Gates et al. reported that Al_2O_3-supported Ir_6 and Ir_4 clusters were catalytically active for toluene[26] and propene[27] hydrogenation. FeO_x-supported single atom Ir catalyst were highly effective for water gas shift reaction.[28] Moreover, Ir nanocrystals (NCs) are also of particular importance as catalysts in the applications of proton-exchange membrane fuel cells[24] and direct ammonia fuel cells.[29]

To achieve higher catalytic activity and utilization efficiency, great effort has been devoted to tuning the shape and size of noble metal nanostructures, because the catalytic performance and stability of catalysts are strongly dependent on the morphology of the NCs in various chemical reactions.[30, 31] Among the various morphologies of metal NCs, dendritic structures have received considerable research interest for their high catalytic activity, owing to their large specific surface area, many high index facets, rich edge and corner atoms.[32-34] Recently, Pt-on-Pd,[35] pure Pd,[36] Pt,[18] Rh,[37] and Au[38] nanodendrites (NDs) have been synthesized and all of them exhibited high-performance electrocatalytic activities. Xia et al. demonstrated that the activity of Pt-on-Pd NDs for oxygen reduction reaction (ORR) was 2.5 times more active than that of the commercial Pt/C catalyst and 5 times more active than Pt-black catalyst.[39] Carbon-supported Pd NDs have been found to be 4.8 times more active for ORR than commercial Pd/C catalyst.[36] Previous literature reported that Ir NCs can be used as important catalysts for CO oxidation[40] and ammonia decomposition,[41] therefore, it is reasonable to expect that Ir NDs with large specific surface area and many high index facets will exhibit unexpected catalytic activities as a catalyst to oxidize CO and decompose ammonia.

Herein, we report a facile one-pot method to synthesize branched Ir NDs based on the oriented attachment mechanism, with primary amine served as the solvent, reductant and ligand. $Fe(OH)_x$-supported Ir NDs catalyst exhibits remarkable CO catalytic activity, and the temperature for full conversion of CO is as low as 120 °C, 40 and 100 °C lower than that of the $Fe(OH)_x$-supported Ir nanoparticles (NPs) and commercial Ir black, respectively. Furthermore, compared to Ir NPs and commercial Ir black, the mass activity of the as-prepared Ir NDs is 7 and 2.6 times higher than that of the both catalysts for ammonia oxidation, respectively. The superior performance of the Ir NDs could be attributed to the large specific surface area, many high index facets, rich edge and corner atoms which are highly desirable for improving the catalytic activity.

Experimental

Materials: Iridium (III) chloride hydrate ($IrCl_3$ 99.9%), trioctylphosphine (TOP, 90%), oleylamine (OLA, ≥ 70%) and iridium black (Ir, 99.8%) were obtained from Alfa Aesar. Hexadecylamine (HDA, ≥ 98%), octadecylamine (ODA, > 90%) were purchased from Fluka. Toluene, methanol, chloroform and acetone were commercially available analytical-grade products. All chemicals used in the experiments were utilized without further purification.

Synthesis of Ir NDs and NPs: typically, $IrCl_3$ (0.33 mmol), ODA (5 mL) were loaded into a 50 mL three-neck flask at ambient environmental conditions. Then the flask was connected to the Schlenk line equipped with a condenser. The equipment was heated gradually to 120 °C, under a nitrogen flow and vigorous magnetic stirring conditions, and was kept at this temperature for 30 min. Then the mixed solution was heated to 290 °C at a rate of 10 °C/min. Aliquots were taken out from the reaction solution at different time intervals for further characterization. Finally, the black precipitate from the reaction solution was isolated by centrifugation at a speed of 13000 r/min and washed with toluene and methanol for three times, and then a trait of chloroform and an excess amount of acetone were added to be washed for another two times. Finally, the products were dissolved in nonpolar solvents forming stable colloidal solutions. Besides, Ir NPs were synthesized by similar procedures to those described for the synthesis of branched Ir NDs except that the solvent was changed to a mixture solution of ODA and TOP with a 1:1 volume ratio.

Characterization: X-ray powder diffractometer (Shimadzu, XRD-6000) operating at 40 kV and 40 mA with Cu Kα radiation was used to record the X-ray diffraction (XRD) patterns of the samples. Data were collected from 30° to 90° with a sampling interval 0.02° per step and a scan speed of 4° per minute. Samples for Transmission electron microscopy (TEM) characterization were prepared by adding several drops of Ir products solution onto the 300-mesh copper grids with carbon support film. TEM, high-resolution transmission electron microscopy (HRTEM) images and selected area electron diffraction (SAED) patterns were acquired with a JEM-2200FS TEM operating at 200 kV. Composition of the specimens was analyzed using energy-dispersive X-ray (EDX) spectroscopy attached to the JEM-2200FS.

Catalysts preparation: The $Fe(OH)_x$-supported Ir catalyst was prepared by a colloid-deposition route. Typically, under stirring at room temperature, a dispersion of the Ir NDs in ethanol was added into an aqueous solution of $Fe(NO_3)_3 \cdot 9H_2O$ and sonicated for 10 min. Afterwards, an excess amount of NaOH aqueous solution was added dropwise to the mixture under stirring. After stirring for 2 h, the resulting precipitate was centrifuged and washed with hot distilled water and then dried at 80 °C for 6 h. The Al_2O_3-, TiO_2- and CeO_2-supported Ir catalysts were prepared by adding a defined amount of corresponding support to a chloroform colloidal solution of Ir NDs. Then, the solution was sonicated for 5 min and dried at 80 °C for 6 h.

Measurements of catalytic activities of CO oxidation: The CO oxidation tests were carried out in a continuous fixed-bed reactor with about 100 mg of a solid catalyst sample (40-60 mesh). The mixture gases for CO oxidation were about 1 vol% CO+10 vol% O_2 balanced with Ar. The total flow rate was 100 mL/min corresponding to a space velocity of 60000 $mLh^{-1}g_{cat}^{-1}$. The concentrations of CO in the effluent gas were analyzed by Shimadzu GC-8A gas chromatography equipped with a thermal conductivity detector. The CO conversion was calculated from the change in CO concentration of the inlet and outlet gases. CO conversion (%) = $\{([CO]_{in} - [CO]_{out})/[CO]_{in}\} \times 100$.

Measurements of electrocatalytic activities of ammonia oxidation: The electrochemical catalytic investigation of the unsupported Ir NDs, Ir NPs and Ir black was carried out with a CHI 660E electrochemical workstation (Shanghai Chenhua Apparatus, China). The working electrode was a catalyst-coated glassy carbon (GC) electrode (d = 3 mm, geometric area 0.07 cm^2). The Pt wire with a diameter of 1 mm and Hg/HgO (CHI, 1 M KOH) were used as the counter and reference electrodes, respectively. To prepare the working electrode, a GC electrode was first polished with alumina slurries (0.05 μm) and then cleaned by sonication in distilled water and ethanol, respectively, for 5 min to remove any alumina residues, and then allowed to dry. 2 mg of Ir NDs or Ir NPs were dispersed in 0.4 mL chloroform and sonicated for 3 min. 2 μL of the catalyst ink was added onto the GC electrode surface by a microliter syringe, then the working electrodes were obtained after the solvent was dried naturally, resulting in a catalyst loading of 10 μg. The loading amount of Ir black for the ammonia catalytic oxidation is the same with Ir NDs. 6 μL of 0.5 wt% nafion solution was dropped on the surface of the above catalysts modified GC and dried naturally before electrochemical experiments. 1 M KOH aqueous solution deoxygenated with purified nitrogen was used as the supporting electrolyte. Ammonia solutions were prepared with ammonia sulfate in 1 M KOH, at different concentrations in the range of 0.005-0.8 M for cyclic voltammetric (CV) curves and 0.1 M for chronoamperometry curves. The potential scan rate was 5 mV/s for the CV measurement. The accelerated durability tests were carried out in N_2-saturated 1 M KOH + 0.1 M NH_3 solutions by applying cyclic potential sweeps between -0.9 and 0 V *versus* Hg/HgO at a sweep rate of 100 mV/s for 1000 and 3000 cycles, respectively. All the experiments were conducted at room temperature.

Results and Discussion

Morphological and Structural Characterization

The detailed synthetic procedures of Ir NDs are described in the experimental section. As the reaction proceeded, the color of the reaction solution was gradually changed from light yellow (250 °C) to black (290 °C), as shown in Fig. S1. TEM images of the as-synthesized product are shown in Fig. 1a, b. The lower magnification image (Fig. 1a) indicates the product is made up of well-dispersed Ir NDs strikingly uniform in both morphology and size. Higher magnification image (Fig. 1b) shows that the well-defined Ir NDs are about 20 nm across composed of smaller particles with diameters of about 3 nm.

Fig. 1 Characterization of Ir NDs prepared by the reduction of $IrCl_3$ in the solution of ODA: (a, b) TEM images of the Ir NDs; (c) powder XRD pattern of the as-prepared Ir NDs; (d) HRTEM image of a single Ir ND; (e) magnified HRTEM image of one arm of the Ir ND (the square area) and (f) the corresponding FFT pattern of the Ir ND shown in (d).

XRD pattern (Fig. 1c) of the Ir NDs is well indexed with the standard JCPDS No.87-0715, indicative of the metallic face-centered cubic (fcc) structure. The EDX of the branched NDs suggests that the obtained nanostructures are completely made up of pure Ir (Fig. S2). The lattice fringes of the dendritic structure, with interconnected arms branching in various directions, are coherently extended across several branches, as shown in Fig. 1d. However, the lattice fringes of a single Ir dendrite are not perfectly aligned across the entire particle, thus the individual Ir ND is polycrystalline, which is further confirmed by the corresponding fast Fourier-transform (FFT) pattern (Fig. 1f) of a complete Ir nanodendrite. The polycrystalline nature of the Ir NDs is attributed to the involvement of twinning and/or imperfect oriented attachment characterized by a small mis-orientation at the interface.[42] The branched polycrystalline Ir NDs possess many crystal facets, edges, corners and a number of atomic steps on their surfaces, as revealed by the HRTEM image (Fig. 1d). HRTEM image collected from one of branches shows obvious lattice fringes with a lattice spacing of 0.22 nm (Fig. 1e), corresponding to that of the (111) plane of Ir.

Investigation of the Formation Mechanism

To investigate the formation mechanism of the Ir NDs, aliquots of the reaction solution were taken out at 1, 2, 5 and 15 min and examined using XRD and TEM analysis. XRD patterns of the products validate that Ir^{3+} is reduced into Ir^0 by the reductant, ODA, at the initial stage (Fig. S3). The decreasing of the full-width at half-maximum of the (111) reflection demonstrates that the size of the Ir NPs increases gradually with the reaction proceeding. In the initial stage, in addition to some of the bud-like NPs, the products mainly contained a large amount of small NPs (Fig. 2a). As the reaction proceeded to 2 min, a number of bud-like Ir NPs appeared, attributed to the self-aggregation of discrete Ir NPs to reduce the surface energy (Fig. 2b). When the reaction proceeded to 5 min, some Ir NDs could be observed owing to the self-aggregation of bud-like Ir NPs (Fig. 2c). After 15 min, essentially all the Ir particles disappeared and evolved into a highly branched structure with an overall dendritic morphology (Fig. 2d). The morphological evolutions combined with the polycrystalline nature of Ir NDs that are composed of several single-crystalline branches indicated that the Ir NDs were formed through oriented attachment formation mechanism,[43] where initially formed small Ir particles self-aggregated, thus they share a common crystallographic orientation. The proposed schematic illustration of self-aggregation based growth mechanism on the formation of Ir NDs is depicted in Fig. 2e. Similar growth mechanism was also reported in the synthesis of Pt NDs.[43] Moreover, the nanostructures of Ir NDs did not exhibit any morphological change during the next 2 h (Fig. S4).

Fig. 2 The shape evolution process of dendritic Ir NCs, proposed schematic of oriented attachment mechanism on the formation of Ir NDs. (a-d) show the time-dependent morphologies at 1, 2, 5, and 15 min, respectively; (e) schematic illustration of the proposed growth mechanism for Ir NDs.

Nanocrystals growth based on the self-aggregation is often observed among small particles, because of their higher energy arising from the large surface-to-volume ratio, higher collision frequency and the reduction in surface energy upon the attachment of particles.[44] It was found that the binding affinity of the ligands have an important effect on both the nucleation and growth stages related to the formation of nanostructures, and thus the final morphologies. Particularly, it was found that ligands with intermediate binding affinity towards Pd^{2+} ions adjust their gradual reduction and contribute to the aggregation-based assembly of the weakly passivated Pd NPs into NDs, while strongly coordinated ligands delay burst-like nucleation, and facilitate growth of quasi-spherical well-passivated NPs through atomic addition.[45] It was observed that ineffective stabilization by the surfactant contributed to coalescence and self-aggregation, which played an important role in the NDs growth. Compared to TOP, ODA is a less effective stabilizer, which has been confirmed previously.[46] Skrabalak et al. found that the formation of Pd dendrites through aggregation-based growth is linked to weak ligand interactions to both Pd^{2+} ions and the generated Pd NPs.[45] Herein, as a weak ligand and reductant, ODA is of significant importance for the formation of Ir NDs in regulating Ir^{3+} gradual reduction and promoting the aggregation-based assembly of the weakly passivated Ir NPs into NDs. In order to confirm our point of view, the effect of the binding affinity of ODA on the formation of Ir NDs was then examined by using a strong binding affinity agent, TOP. Fig. S5a depicts the TEM image of Ir NPs prepared in a mixed solution of ODA and TOP. It can be seen that the product was composed of relatively uniform spherical NPs with a diameter of about 3 nm. The HRTEM image (Fig. S5b) and XRD (Fig. S5c) pattern of the Ir NPs confirm the fcc crystal structure of the Ir NPs, which is consistent with the SAED result (Fig. S5d). Moreover, in order to investigate the effect of the carbon chain on the morphology of the Ir NPs, explorations were also carried out by replacing ODA with HDA or OLA. Fig. S6 shows the TEM images of the product obtained with HDA, OLA and ODA as solvents, respectively. In the case of HDA, the morphology and size of the product are similar to those obtained with ODA, owing to the similar structures of HDA and ODA except that the carbon chain length of HDA is shorter than that of ODA. However, in the case of OLA, the product consists of larger NDs with a size of about 30 nm and small NPs of about 4 nm in size, resulting from the C=C bond in the OLA, which has been confirmed that the bond

Fig. 3 (a) Catalytic activities of CO oxidation on $Fe(OH)_x$-, Al_2O_3-, TiO_2-, and CeO_2-supported Ir NDs and $Fe(OH)_x$-supported commercial Ir black catalysts; (b) conversion of CO as a function of reaction temperature over pure $Fe(OH)_x$ and $Fe(OH)_x$-supported Ir NDs catalysts with different Ir loading. Reaction conditions: 1 vol% CO, 10 vol% O_2, and balance Ar. Weight hourly space velocity (WHSV): 60000 $mLh^{-1}g_{cat}^{-1}$.

strength of $[Au(CH_2{=}AuCH_2)]^+$ is larger than that of $[Au(NH_3)]^+$.[47] In the present reaction system, the precursor concentrations have also an effect on the shape of the Ir NDs. A low Ir precursor concentration gives rise to irregular NPs with bud-like dendritic structures, whereas higher Ir precursor concentration is favorable for facilitating the production of dendritic nanostructures (Fig. S7). In addition, it was found that temperature had a limited effect on the resulting morphologies of the Ir nanostructures in this system, as shown in Fig. S8.

Catalytic Oxidation of CO

Metal NPs supported on transition-metal oxides are used not only to obtain a beneficial dispersion of metal NPs but also to shift the main task of the support from ensuring sufficient particle dispersion to participating in the catalytic reaction. Many transition-metal oxides, such as TiO_2,[48] CeO_2[49] and Fe_3O_4,[50] have been proven to show a strong metal-support interactions (SMSI) effect which can strongly influence the electronic structure of metal catalysts and thus the catalytic performance. $Fe(OH)_x$, as a support, which was wildly used to disperse metal NPs, has been confirmed to effectively enhance catalytic activity.[51] As a consequence, the contribution of the support to the catalytic activity of the catalyst should be taken into account. In the present research, we studied the performance of catalytic oxidation of CO about $Fe(OH)_x$-, Al_2O_3-, TiO_2- and CeO_2-supported Ir NDs catalysts by temperature-programmed method. To better investigate the catalytic effect of the Ir NDs on CO oxidation, $Fe(OH)_x$-supported commercial Ir black catalyst with a 4 wt% Ir loading (denoted as IrbFe4) was selected as a reference to compare their catalytic properties. Fig. 3a shows the profiles of CO conversions as a function of reaction temperature for the $Fe(OH)_x$-, Al_2O_3-, TiO_2- and CeO_2-supported Ir NDs and $Fe(OH)_x$-supported Ir black catalysts with a 4 wt% Ir loading (denoted as IrFe4, IrAl4, IrTi4, IrCe4 and IrbFe4, respectively). At lower temperature (< 100 °C), all of the catalysts show a similar inferior catalytic activity. The CO conversion is only about 20% at 160 °C for IrbFe4 and the temperature for 100% CO conversion towards this sample is up to 220 °C. However, a sudden jump could be observed for IrFe4 and IrAl4 at temperatures more than 100 and 160 °C, respectively. This is attributed to the fact that organic ligands would tune strong metal-support interaction for CO catalytic oxidation[50] for our present ODA capped Ir NDs. Compared to Ir NDs deposited on chemically inert metal oxide supports, $Fe(OH)_x$-supported Ir NDs catalyst perform better with a full conversion of CO at 120 °C. Therefore, in the following experiment, we focused on $Fe(OH)_x$-supported Ir catalysts as the main object of study. As a comparison, we also tested the activity of $Fe(OH)_x$-supported Ir NPs with a 4 wt% Ir loadings (denoted as Ir-PFe4) for the CO oxidation, as shown in Fig. S9. The sudden jump of IrFe4 occurs at T = 100 °C which is 40 °C lower than that of Ir-PFe4. This is owing to dendritic structure of Ir NDs possessing larger specific surface area, many high index facets, rich edge and corner atoms. It is well known that the metallic nature of metal NCs supported on transition-metal oxides plays an important role in improving catalytic activity. In addition, Gracia et al. found that fully oxidized Pt particles exhibited low activity for CO oxidation.[52] Fig. S10 shows the TEM and HRTEM images of the as-prepared IrFe4, suggesting that the shape, size and metallic nature of Ir NDs had no obvious change after drying at 80 °C for 6 h. The metallic nature of Ir NDs in the IrFe4 may be another reason for its high performance in CO oxidation. Fig. 3b illustrates the profiles of CO conversions for the $Fe(OH)_x$-supported Ir NDs catalysts with a 2.5 wt%, 1 wt% Ir loading (denoted as IrFe2.5 and IrFe1, respectively) and pure $Fe(OH)_x$. We can observed that, under the experimental conditions, pure $Fe(OH)_x$ itself had a lower activity for the oxidation of CO to CO_2. However, the IrFe2.5 and IrFe1 exhibited comparable levels of activity in the oxidation of CO and the temperature for fully CO conversion increased to 180 °C. This result indicated that the temperature ranges for the total conversion of CO could be adjusted, to a certain extent, by varying the loading of Ir NDs. It also suggested that Ir NDs affect the behavior and performance of the catalysts.

Fig. 4 Cyclic voltammograms of Ir NDs and Ir NPs catalysts recorded in N_2-saturated 1 M KOH + 0.1 M NH_3 aqueous solution with a sweep rate of 5 mV/s. Inset: the mass activity of Ir NDs and Ir NPs.

Fig. 5 (a) cyclic voltammograms of Ir NDs in 1 M KOH + 0.1 M NH_3 aqueous solution with different scan rate; (b) the peak current density as a function of square root of the potential scan rate.

Electrocatalytic Oxidation of Ammonia

Electrochemical oxidation of ammonia received particular interest from the viewpoint of potential application in direct ammonia fuel cells and hydrogen production. Thereby, we studied the electrocatalytic activities of the as-prepared products toward ammonia oxidation by an electrochemical workstation. Fig. 4 shows the cyclic voltammograms of the Ir NDs and NPs recorded at room temperature in N_2-saturated 1 M KOH + 0.1 M NH_3 solution with potential scanned from -0.9 to 0 V *versus* Hg/HgO, at a sweep rate of 5 mV/s. Well marked anodic peaks in the forward sweeps, associated with the oxidation of ammonia, could be observed for both catalysts at about -0.35 V.[53] The oxidation current values were normalized with respect to electrochemically active surface areas, which were calculated by measuring the amount of charges involved in the hydrogen adsorption/desorption region after double-layer correction and assuming a value of 218 $\mu C/cm^2$ for the adsorption of a hydrogen monolayer. The specific ECSA (the ECSA per unit weight of metal) of Ir NDs is 30.9 m^2/Ir_g, much higher than that of Ir NPs (7.4 m^2/Ir_g) and Ir black (2.8 m^2/Ir_g), respectively. The extensive agglomeration of Ir black should be account for their small specific ECSA (Fig. S11). For Ir NDs, not only the specific activity (i.e., peak current of ammonia oxidation per unit surface area of catalyst) of ammonia oxidation (0.042 mA/cm^2) is much higher than that of the Ir NPs (0.024 mA/cm^2), but also the oxidation starts at a more negative potential (-0.35 V) than that of Ir NPs (-0.31 V), which highlights the high ammonia oxidation activity of the Ir NDs catalyst. Furthermore, the Ir NDs have a higher mass activity which is 7 and 2.6 times higher than that of the Ir NPs and Ir black (Fig. 4 inset and Fig. S12). Compared with Ir NDs, well marked anodic peaks in the forward sweeps, associated with the oxidation of Ir black, could be observed at -0.25 V. Therefore, the obtained oxidation current of ammonia

Fig. 6 (a) Cyclic voltammograms of Ir NDs catalyst before and after 1000 and 3000 cycles; (b) chronoamperometric results of ammonia oxidation at different potentials on Ir NDs catalyst in N_2-saturated 1 M KOH + 0.1 M NH_3 aqueous solution. The durability tests were performed in N_2-saturated 1 M KOH + 0.1 M NH_3 aqueous solution at a scan rate of 100 mV/s between -0.9 and 0 V *versus* Hg/HgO.

over Ir black should contain the contribution of the oxidation of catalyst itself, and thus the actual mass activity of Ir black for ammonia oxidation should be lower than 5 mA/mg. The reason for the excellent activity of Ir NDs catalyst for ammonia oxidation should be due to their large specific area, many high index facets, rich edge and corner atoms.[54] The effect of ammonia concentration on the electrocatalytic activity of Ir NDs is shown in Fig. S13. Ammonia oxidation peak current density at around -0.35 V increases up to the maximum at 0.3 M NH_3, and then it decreases with increasing ammonia concentration. This behavior could be accounted for the rate of N_{ads} (nitrogen adsorbates) formation increases with the increase of ammonia concentration, and thus ultimately poisoning Ir NDs catalyst.[55] Fig. 5a presents the cyclic voltammograms of Ir NDs catalyst in 1 M KOH + 0.1 M NH_3 solution at different potential sweep rates. The ammonia oxidation current density at about -0.35 V increase significantly with the increase of potential sweep rate. The peak potentials at around -0.35 V are almost independent of the potential sweep rate and the difference is close to 43 mV. An expression associated with the current response to the potential sweep rate was given by Gabrielli et al.[56] The peak current density follows a linear $\upsilon^{1/2}$ (υ: potential sweep rate) dependence (Fig. 5b), indicating the diffusion controlled processes of the ammonia oxidation reaction.[57]

The ammonia oxidation stability of the Ir NDs catalyst was investigated by potential cycling between -0.9 and 0 V in N_2-saturated 1 M KOH + 0.1 M NH_3 aqueous solutions, with scan rate of 100 mV/s. After 1000 and 3000 cycles the peak current densities of the Ir NDs still remained 0.038 and 0.030 mA/cm^2, corresponding to an activity loss of 8.6% and 28.7%, respectively, which indicated the high stability of Ir NDs catalyst (Fig. 6a). The long term stability of Ir NDs toward ammonia oxidation was also evaluated through the chronoamperometric measurements at various potentials in 1 M KOH + 0.1 M NH_3 aqueous solutions, as shown in Fig. 6b. Although the current density of Ir NDs at -0.29 V *versus* Hg/HgO was much higher at the beginning, it decreased rapidly and higher current density was obtained at -0.41 V *versus* Hg/HgO after 131 seconds. Chronoamperometric testing confirms the higher stability of the Ir NDs catalyst at the potential of -0.41 V *versus* Hg/HgO. It is possible that NH_x (x = 1 or 2) cannot be oxidized completely to produce N_2 at a more negative potential, while at a more positive potential, the main adsorbates becomes N_{ads} and both cases block catalyst active sites. At the same potential, the specific activity of the Ir NDs is still higher than that of the Ir NPs after 1000 s (Fig. S14). These results indicate that the Ir NDs have higher electrocatalytic activity and stability than the Ir NPs toward ammonia oxidation.

Conclusion

In conclusion, we have demonstrated a simple method for one-pot synthesis of Ir NDs based on the oriented attachment mechanism. Ir NPs was also prepared by using a strong ligand in the reaction solution. Reaction parameters (precursor concentration, reaction temperature) have little effect on the shape and size of Ir NDs. Compared to Fe(OH)$_x$-supported Ir NPs and Ir black, Ir NDs on the identical support exhibit enhanced activity for CO oxidation with a full conversion of CO at 120 °C. Moreover, the mass activity of Ir NDs is 7 and 2.6 times higher, respectively, than that of Ir NPs and Ir black for ammonia electrocatalytic oxidation. The higher catalytic activities of Ir NDs are owing to their large specific surface area, many high-index facets and rich edge and corner atoms. We expect that the Ir NDs are a promising candidate for the potential application in proton-exchange membrane fuel cells and direct ammonia fuel cells.

Ackonwledgements

We thank Mr. Lingwei (Willian) Kong (Pembroke Pines Charter High School, Miami) for English polish. This work was supported by NSFC (Nos. 91227202, 51202086 and 11404135), RFDP (Nos. 20120061130006 and 20110061120014), the National Basic Research Program of China (No. 2011CB808200), and the China Postdoctoral Science Foundation (Nos. 2013T60325 and 2014M550171).

Notes and references

[a] *State Key Laboratory of Superhard Materials, Jilin University, Changchun 130012, P. R. China. E-mail: zoubo@jlu.edu.cn; suiym@jlu.edu.cn*
[b] *State Key Laboratory of Theoretical and Computational Chemistry, College of Chemistry, Jilin University, Changchun 130021, P. R. China.*
[c] *College of Physics, Jilin University, Changchun 130012, P. R. China.*

† Electronic Supplementary Information (ESI) available: See DOI: 10.1039/b000000x/

1. S. Jeong, K. Woo, D. Kim, S. Lim, J. S. Kim, H. Shin, Y. N. Xia and J. Moon, *Adv. Funct. Mater.* 2008, **18**, 679-686.
2. H. H. Wang, Z. H. Sun, Q. H. Lu, F. W. Zeng and D. S. Su, *Small* 2012, **8**, 1167-1172.
3. T. A. Taton, C. A. Mirkin and R. L. Letsinger, *Science* 2000, **289**, 1757-1760.
4. S. E. Skrabalak, J. Chen, L. Au, X. M. Lu, X. D. Li and Y. N. Xia, *Adv. Mater.* 2007, **19**, 3177-3184.
5. J. Y. Chen, B. Wiley, Z. Y. Li, D. Campbell, F. Saeki, H. Cang, L. Au, J. Lee, X. D. Li and Y. N. Xia, *Adv. Mater.* 2005, **17**, 2255-2261.
6. X. M. Yang, S. E. Skrabalak, Z. Y. Li, Y. N. Xia and L. V. Wang, *Nano Lett.* 2007, **7**, 3798-3802.
7. Y. H. Kim, J. Jeon, S. H. Hong, W. K. Rhim, Y. S. Lee, H. Youn, J. K. Chung, M. C. Lee, D. S. Lee, K. W. Kang and J. M. Nam, *Small* 2011, **7**, 2052-2060.
8. P. H. Zhang, Y. M. Sui, G. J. Xiao, Y. N. Wang, C. Z. Wang, B. B. Liu, G. T. Zou and B. Zou, *J. Mater. Chem. A* 2013, **1**, 1632-1638.
9. P. H. Zhang, Y. M. Sui, C. Wang, Y. N. Wang, G. L. Cui, C. Z. Wang, B. B. Liu and B. Zou, *Nanoscale* 2014, **6**, 5343-5350.
10. L. Wang, Y. Nemoto and Y. Yamauchi, *J. Am. Chem. Soc.* 2011, **133**, 9674-9677.
11. G. Lu, S. Z. Li, Z. Guo, O. K. Farha, B. G. Hauser, X. Y. Qi, Y. Wang, X. Wang, S. Y. Han, X. G. Liu, J. S. DuChene, H. Zhang, Q. C. Zhang, X. D. Chen, J. Ma, S. C. J. Loo, W. D. Wei, Y. H. Yang, J. T. Hupp and F. W. Huo, *Nat. Chem.* 2012, **4**, 310-316.
12. Y. Y. Cai, X. H. Li, Y. N. Zhang, X. Wei, K. X. Wang and J. S. Chen, *Angew. Chem. Int. Ed.* 2013, **52**, 11822-11825.
13. N. Tian, Z. Y. Zhou, N. F. Yu, L. Y. Wang and S. G. Sun, *J. Am. Chem. Soc.* 2010, **132**, 7580-7581.

14. P. Hauwert, G. Maestri, J. W. Sprengers, M. Catellani and C. J. Elsevier, *Angew. Chem. Int. Ed.* 2008, **47**, 3223-3226.
15. S. H. Joo, J. Y. Park, J. R. Renzas, D. R. Butcher, W. Huang and G. A. Somorjai, *Nano Lett.* 2010, **10**, 2709-2713.
16. T. Hayashi and K. Yamasaki, *Chem. Rev.* 2003, **103**, 2829-2844.
17. A. M. Argo, J. F. Odzak, J. F. Goellner, F. S. Lai, F. S. Xiao and B. C. Gates, *J. Phys. Chem. B* 2006, **110**, 1775-1786.
18. M. A. Mahmoud, C. E. Tabor, M. A. El-Sayed, Y. Ding and Z. L. Wang, *J. Am. Chem. Soc.* 2008, **130**, 4590-4591.
19. S. H. Sun, G. X. Zhang, D. S. Geng, Y. G. Chen, R. Y. Li, M. Cai and X. L. Sun, *Angew. Chem. Int. Ed.* 2011, **50**, 422-426.
20. Y. Q. Zheng, J. Tao, H. Y. Liu, J. Zeng, T. Yu, Y. Y. Ma, C. Moran, L. J. Wu, Y. M. Zhu, J. Y. Liu and Y. N. Xia, *Small* 2011, **7**, 2307-2312.
21. F. Liu, J. Y. Lee and W. J. Zhou, *Small* 2006, **2**, 121-128.
22. G. Helmchen, A. Dahnz, P. Dubon, M. Schelwies and R. Weihofen, *Chem. Commun.* 2007, 675-691.
23. M. Gartner, S. Mader, K. Seehafer and G. Helmchen, *J. Am. Chem. Soc.* 2011, **133**, 2072-2075.
24. J. Lin, B. T. Qiao, J. Y. Liu, Y. Q. Huang, A. Q. Wang, L. Li, W. S. Zhang, L. F. Allard, X. D. Wang and T. Zhang, *Angew. Chem. Int. Ed.* 2012, **51**, 2920-2924.
25. W. S. Zhang, Y. Q. Huang, J. H. Wang, K. Liu, X. D. Wang, A. Q. Wang and T. Zhang, *Int. J. Hydrogen Energy* 2010, **35**, 3065-3071.
26. A. Zhao and B. Gates, *J. Am. Chem. Soc.* 1996, **118**, 2458-2469.
27. G. Panjabi, A. M. Argo and B. C. Gates, *Chem.-Eur. J.* 1999, **5**, 2417-2423.
28. J. Lin, A. Q. Wang, B. T. Qiao, X. Y. Liu, X. F. Yang, X. D. Wang, J. X. Liang, J. Li, J. Y. Liu and T. Zhang, *J. Am. Chem. Soc.* 2013, **135**, 15314-15317.
29. M. Cooper and G. G. Botte, *J. Electrochem. Soc.* 2006, **153**, A1894-A1901.
30. D. Kim, Y. W. Lee, S. B. Lee and S. W. Han, *Angew. Chem. Int. Ed.* 2012, **51**, 159-163.
31. Y. N. Xia, Y. J. Xiong, B. Lim and S. E. Skrabalak, *Angew. Chem. Int. Ed.* 2009, **48**, 60-103.
32. X. W. Teng, X. Y. Liang, S. Maksimuk and H. Yang, *Small* 2006, **2**, 249-253.
33. A. Mohanty, N. Garg and R. C. Jin, *Angew. Chem. Int. Ed.* 2010, **49**, 4962-4966.
34. Q. M. Shen, L. P. Jiang, H. Zhang, Q. H. Min, W. H. Hou and J. J. Zhu, *J. Phys. Chem. C* 2008, **112**, 16385-16392.
35. Z. M. Peng and H. Yang, *J. Am. Chem. Soc.* 2009, **131**, 7542-7543.
36. Q. Gao, M. R. Gao, J. W. Liu, M. Y. Chen, C. H. Cui, H. H. Li and S. H. Yu, *Nanoscale* 2013, **5**, 3202-3207.
37. Y. Feng, X. H. Ma, L. Han, Z. J. Peng and J. Yang, *Nanoscale* 2014, **6**, 6173-6179.
38. X. R. Li, X. L. Li, M. C. Xu, J. J. Xu and H. Y. Chen, *J. Mater. Chem. A* 2014, **2**, 1697-1703.
39. B. Lim, M. J. Jiang, P. H. Camargo, E. C. Cho, J. Tao, X. M. Lu, Y. M. Zhu and Y. N. Xia, *Science* 2009, **324**, 1302-1305.
40. M. Okumura, N. Masuyama, E. Konishi, S. Ichikawa and T. Akita, *J. Catal.* 2002, **208**, 485-489.
41. A. De Vooys, M. Koper, R. Van Santen and J. Van Veen, *J. Electroanal. Chem.* 2001, **506**, 127-137.
42. B. Lim and Y. N. Xia, *Angew. Chem. Int. Ed.* 2011, **50**, 76-85.
43. B. Lim, M. J. Jiang, T. Yu, P. H. C. Camargo and Y. N. Xia, *Nano Research* 2010, **3**, 69-80.
44. H. M. Zheng, R. K. Smith, Y. W. Jun, C. Kisielowski, U. Dahmen and A. P. Alivisatos, *Science* 2009, **324**, 1309-1312.
45. N. Ortiz and S. E. Skrabalak, *Angew. Chem. Int. Ed.* 2012, **51**, 11757-11761.
46. F. Knittel, E. Gravel, E. Cassette, T. Pons, F. Pillon, B. Dubertret and E. Doris, *Nano Lett.* 2013, **13**, 5075-5078.
47. Y. Y. Ma, J. Zeng, W. Y. Li, M. McKiernan, Z. X. Xie and Y. N. Xia, *Adv. Mater.* 2010, **22**, 1930-1934.
48. S. J. Tauster, *Acc. Chem. Res.* 1987, **20**, 389-394.
49. D. R. Mullins and K. Z. Zhang, *Surf. Sci.* 2002, **513**, 163-173.
50. P. Sonstrom, D. Arndt, X. D. Wang, V. Zielasek and M. Baumer, *Angew. Chem. Int. Ed.* 2011, **50**, 3888-3891.
51. A. A. Herzing, C. J. Kiely, A. F. Carley, P. Landon and G. J. Hutchings, *Science* 2008, **321**, 1331-1335.
52. F. J. Gracia, J. T. Miller, A. J. Kropf and E. E. Wolf, *J. Catal.* 2002, **209**, 341-354.
53. F. J. Vidal-Iglesias, J. Solla-Gullón, V. Montiel, J. M. Feliu and A. Aldaz, *J. Power Sources* 2007, **171**, 448-456.
54. J. Liu, W. B. Hu, C. Zhong and Y. F. Cheng, *J. Power Sources* 2013, **223**, 165-174.
55. T. L. Lomocso and E. A. Baranova, *Electrochim. Acta* 2011, **56**, 8551-8558.
56. C. Gabrielli, M. Keddam, H. Takenouti, V. Quang Kinh and F. Bourelier, *Electrochim. Acta* 1979, **24**, 61-65.
57. L. Zhou and Y. F. Cheng, *Int. J. Hydrogen Energy* 2008, **33**, 5897-5904.